Analysis of Local Seismic Events near a Large-*N* Array for Moho Reflections

Qicheng Zeng[*1] and Robert L. Nowack[1]

Abstract

Local seismic events recorded by the large-*N* Incorporated Research Institutions for Seismology Community Wavefield Experiment in Oklahoma are used to estimate Moho reflections near the array. For events within 50 km of the center of the array, normal moveout corrections and receiver stacking are applied to identify the *PmP* and *SmS* Moho reflections on the vertical and transverse components. Corrections for the reported focal depths are applied to a uniform event depth. To stack signals from multiple events, further static corrections of the envelopes of the Moho reflected arrivals from the individual event stacks are applied. The multiple-event stacks are then used to estimate the pre-critical *PmP* and *SmS* arrivals, and an average Poisson's ratio of 1.77 ± 0.02 was found for the crust near the array. Using a modified Oklahoma Geological Survey (OGS) velocity model with this Poisson's ratio, the time-to-depth converted *PmP* and *SmS* arrivals resulted in a Moho depth of 41 ± 0.6 km. The modeling of wide-angle Moho reflections for selected events at epicenter-to-station distances of 90–135 km provides additional constraints, and assuming the modified OGS model, a Moho depth of 40 ± 1 km was inferred. The difference between the pre-critical and wide-angle Moho estimates could result from some lateral variability between the array and the wide-angle events. However, both estimates are slightly shallower than the original OGS model Moho depth of 42 km, and this could also result from a somewhat faster lower crust. This study shows that local seismic events, including induced events, can be utilized to estimate properties and structure of the crust, which, in turn, can be used to better understand the tectonics of a given region. The recording of local seismicity on large-*N* arrays provides increased lateral phase coherence for the better identification of precritical and wide-angle reflected arrivals.

Cite this article as Zeng, Q., and R. L. Nowack (2020). Analysis of Local Seismic Events near a Large-*N* Array for Moho Reflections, *Seismol. Res. Lett.* **XX**, 1–13, doi: 10.1785/0220200087.

Supplemental Material

Introduction

New advances in seismic instrumentations have made it possible to deploy arrays with a large number of seismometers (large-*N* arrays). The seismic sensors used in these large-*N* experiments are small, inexpensive systems that allow for fast deployments and incorporate a geophone, a data logger, a GPS clock, and power (Freed, 2008; Karplus and Schmandt, 2018; Ringler *et al.*, 2018). Some of the first academic applications of large-*N* arrays used single-component seismic nodes, including experiments conducted near Long Beach, California (Lin *et al.*, 2013; Schmandt and Clayton, 2013; Nakata *et al.*, 2015; Riahi and Gerstoft, 2015; Z. Li *et al.*, 2018), Mount Saint Helens (Hansen and Schmandt, 2015; Hansen *et al.*, 2016; Kiser *et al.*, 2016, 2019; Wang *et al.*, 2017; Glasgow *et al.*, 2018), and along the San Jacinto fault zone (Hillers *et al.*, 2016; Roux *et al.*, 2016). Recent seismic studies involving three-component nodes have also demonstrated the wide application of large-*N* arrays for the fault zones (Qin *et al.*, 2018; Y. Wang *et al.*, 2019), for geothermal areas (Brenguier *et al.*, 2016; Ward and Lin, 2017; Wu *et al.*, 2017), for earthquake mechanism studies (Fan and McGuire, 2018), and for the analysis of cultural signals (C. Li *et al.*, 2018).

A number of array-based approaches have been used to study seismic body waves from the Moho, including controlled-source wide-angle reflection and refraction methods (e.g., Cook *et al.*, 2010; Prodehl and Mooney, 2012; Carbonell *et al.*, 2013). The *PmP* and *SmS* phases from earthquake sources have also been recorded on dense arrays being used for active-source studies, for example, by Mechie *et al.* (2012) for determining crustal *S*-velocities and Poisson's ratio along the INDEPTH IV profile in northeast Tibet. Mori and Helmberger (1996) used closely spaced aftershocks from the 1992 Landers earthquake in southern California to observe

1. Department of Earth, Atmospheric, and Planetary Sciences, Purdue University, West Lafayette, Indiana, U.S.A.

*Corresponding author: qczeng95@gmail.com

SmS Moho reflections. Wang *et al.* (2018) used measurements of *P* and *PmP* arrivals from aftershocks and local earthquakes to perform crustal tomography in western Japan. Griffin *et al.* (2011) investigated the velocity structure of the Tibetan Lithosphere using travel times from *P* and *PmP* arrivals from regional earthquakes recorded on the large-scale Hi-CLIMB array.

Array-based methods have also been applied for seismic receiver functions from teleseismic earthquakes (e.g., Levander and Nolet, 2005; Rondenay, 2009; Nowack *et al.*, 2010). Virtual deep seismic sounding using the *SsPmp* phases has been used for array-based imaging of the crust and Moho from earthquake sources (Tseng *et al.*, 2009; Yu *et al.*, 2013; Thompson *et al.*, 2019). Seismic interferometry has also been applied to teleseismic earthquake sources recorded by seismic arrays using global-phase seismic interferometry (Ruigrok and Wapenaar, 2012; Nishitsuji *et al.*, 2016).

Shen and Ritzwoller (2016) utilized observations from ambient noise and earthquakes, receiver functions and Rayleigh wave ellipticity using the USArray transportable array to study the crust and upper mantle beneath the continental United States, including the broader features beneath Oklahoma. Evanzia *et al.* (2014) conducted V_P and V_S tomography of the crust and upper mantle beneath Texas and Oklahoma, and Zhu (2018) performed tomography of ambient noise for crustal structure of North Texas and Oklahoma. In these studies, features in southern, eastern, and southwestern Oklahoma including the Anadarko basin, Wichita uplift, the Arkoma basin, and the Ouachita uplift could be observed in the tomographic images.

A state-wide velocity model in Oklahoma was developed by Marsh (2018) using ambient noise tomography down to about 20 km in depth, where slower regions were associated with basin structures and faster regions with shallower basement. Ratre and Behm (2019) developed a 3D model of central Oklahoma from the combination of 1D travel-time curves resulting from the stacking and inversion of *Pg* waveforms. They found a generally homogeneous crust with some velocity variations related to regional geological structures. They also estimated a higher speed lower crust, inferring a more mafic lower crust, and used this to assess the extent of the mid-continent rift in Oklahoma. Pei *et al.* (2018) performed *Pg* tomography with anisotropy to investigate crustal seismogenic features in central Oklahoma and correlated these with recent seismic activity. Z. Wang *et al.* (2019) applied *P*-to-*S* receiver functions from teleseismic earthquakes to investigate the crust of Oklahoma.

Inamori *et al.* (1992) utilized seismic reflection methods to image mid-crustal structure using aftershock waveforms from the 1984 Western Nagano Prefecture earthquake in Japan. Quiros *et al.* (2017) applied reflection imaging of aftershocks from the 2011 M_w 5.8 Virginia earthquake recorded by several dense seismic arrays to image crustal reflections. Vertical seismic profiling (VSP) was utilized for earthquake events followed by VSP-Common Reflection Point (VSP-CRP) transformations to account for offset and depth of the events. Eddy and Harder (2018) investigated the correlation of local earthquakes from the Incorporated Research Institutions for Seismology (IRIS) Community Wavefield Experiment in northcentral Oklahoma to form a reflection image of reflectors in the basement and sedimentary section.

In this study, later arrivals from frequent local seismic events near the IRIS Community Wavefield Experiment in Oklahoma (Anderson *et al.*, 2016; Sweet *et al.*, 2018) are used to estimate Moho reflections and crustal Poisson's ratio near the array. This is followed by a normal moveout correction and stacking to an equivalent zero offset. Laterally homogeneous velocities and Moho depth in the vicinity of the array are assumed, with static corrections applied to account for small velocity variability and uncertainties in the earthquake locations. Because the event depths are much shallower than the Moho depth, a reflection methodology is applied rather than full VSP processing.

Seismic events, with locations from the Oklahoma Geological Survey earthquake catalog (OGS Earthquake Catalog, 2016; Walter, *et al.*, 2020) near the array, are utilized. Waveform-relocation and template-matching studies have also been performed by Schoenball and Ellsworth (2017) and Skoumal *et al.* (2019). Many of the seismic events in Oklahoma are now identified as induced events from oil and gas activities, and, in particular, from waste water injection (Ellsworth, 2013; Keranen *et al.*, 2014; Walsh and Zoback, 2015; Weingarten *et al.*, 2015; Langenbruch and Zoback, 2016; Hincks *et al.*, 2018).

We first analyzed the *P*- and *S*-wave later arrivals on the vertical and transverse components for selected events within 50 km from the center of the array. We identified the Moho reflections on the vertical and transverse components for individual events, by applying normal moveout corrections and receiver stacking. *P*-wave and *S*-wave Moho reflection signals were enhanced by multiple-event stacking after static corrections, and polarity sign corrections were applied. These stacks were then used to infer average crustal V_P/V_S ratio, Poisson's ratio, and Moho depth near the array. We also modeled wide-angle *PmP* and *SmS* Moho reflections for selected events at epicenter-to-station distances of 90–135 km, which provides additional constraints. The analysis of local seismicity, including induced seismicity in areas with less natural seismicity, can be used to estimate the properties and structure of the crust, which, in turn, can be utilized to better understand the tectonics of a given region. The recording of local seismicity on large-*N* arrays allows for increased lateral phase coherence for the better identification of smaller seismic arrivals.

Seismic Data

The seismic data used in this study are selected from the OGS earthquake catalog from 24 June to 20 July 2016 (OGS Earthquake Catalog, 2016). The seismic events were recorded by the seismic stations of IRIS Community Wavefield

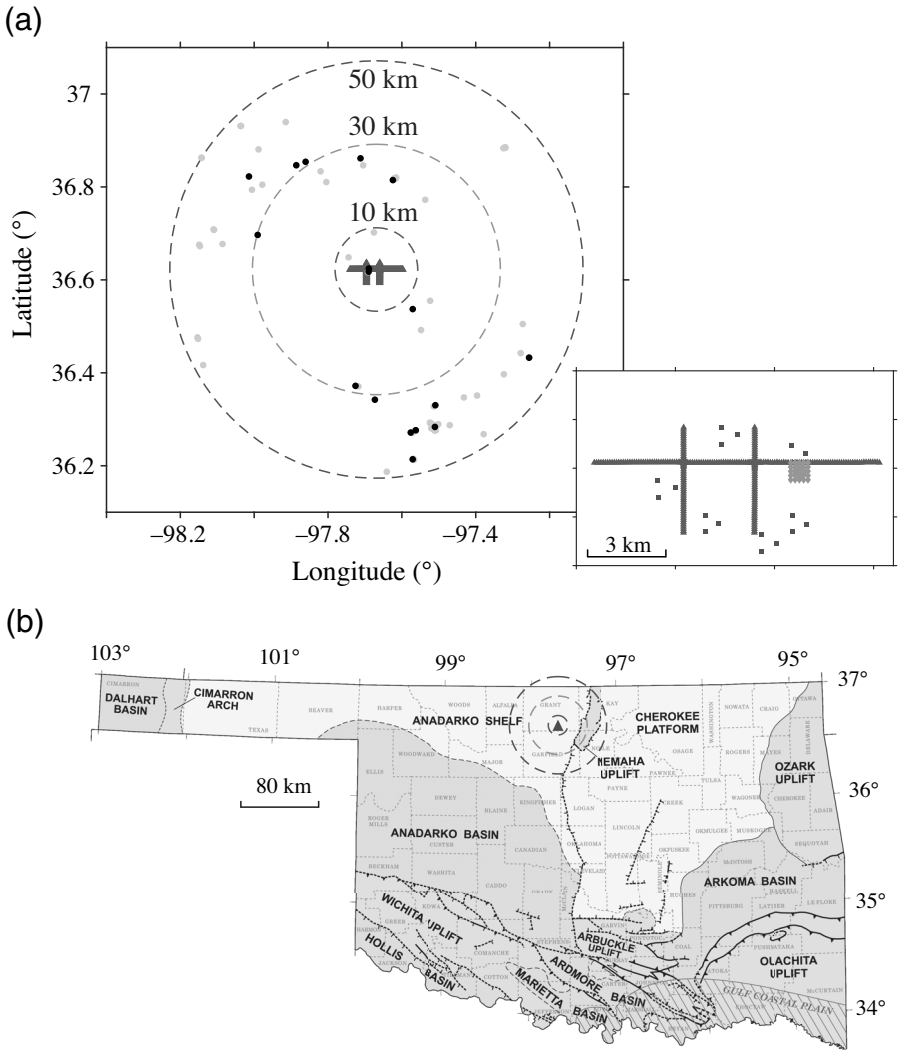

Figure 1. (a) Map of near offset seismic events from the Oklahoma Geological Survey (OGS) earthquake catalog over a period from 24 June to 20 July 2016. The events are denoted by dots, and the dark black dots were selected for the analysis. Dashed circles have radii of 10, 30, and 50 km from a central station of the array of the Incorporated Research Institutions for Seismology (IRIS) Community Wavefield Experiment. The right inset map shows the geometry of the receivers in the array. Triangles are the north–south and east–west linear nodal array stations, the small square denotes stations from the nodal gradiometer array, and the black squares are the broadband stations (Sweet *et al.*, 2018). (b) Major geologic structures in Oklahoma (adapted from Johnson 2008). The triangle in north-central Oklahoma denotes the location of the array. Dashed circles around the triangle have radii of 10, 30, and 50 km from a central station of the array.

Experiment in Oklahoma. Figure 1a shows the locations of seismic events with epicenters less than 50 km from the center of the array. Selected events in this distance range are then used to investigate *P*- and *S*-wave Moho reflections. The seismic array and a 50 km radius region around it, including the selected events, are also shown in Figure 1b, along with the major geological features in Oklahoma (Johnson, 2008).

The IRIS Community Wavefield Experiment included 363 nodal sensors deployed along three lines, a seven-layer gradiometer nodal array, and 18 broadband stations collocated with nine infrasound stations (Sweet *et al.*, 2018). The nodes deployed in this experiment were Z-Land Fairfield nodal 5 Hz three-component sensors with ~35 days of battery life and a 250 samples/second sampling rate.

The right inset of Figure 1a shows the geometry of the seismometers in the array. The triangles are the north–south and east–west linear nodal array stations; the diamonds denote stations from the nodal gradiometer array. The spacing between the nodes along the north–south and east–west lines was about 100 m. The length of the east–west line is about 13 km, and the length of the north-south lines are about 5 km. The linear array nodal sensors were deployed from 20 June to 20 July for about 30 days (Sweet *et al.*, 2018). The squares are the 18 broadband stations, which were deployed from 20 June to 10 November 2016 for about five months. For this study, the east–west linear nodal array stations were utilized to analyze the seismic events near the array.

A reference velocity model for Oklahoma from the OGS (Darold *et al.*, 2015) is shown in Figure 2 and is denoted by solid lines, with the *S*-wave velocities on the left and *P*-wave velocities on the right. The OGS velocity model assumes a constant 1.73 V_P/V_S ratio. A modified *S*-velocity model with a V_P/V_S ratio of 1.77 obtained from the analysis of *PmP* and *SmS* arrivals in this study is also shown in Figure 2, denoted by the dashed line. For comparison, the velocity model for locations near the array from CRUST1.0 (Laske *et al.*, 2013) is also shown in Figure 2 by the dotted lines. The depth of the Moho is at 42 km for the OGS velocity model and also for CRUST1.0 in the region near the array.

Moveout Analysis

Alignment of Moho reflected seismic signals is performed to enhance the signal-to-noise ratio. Figure 3 illustrates the

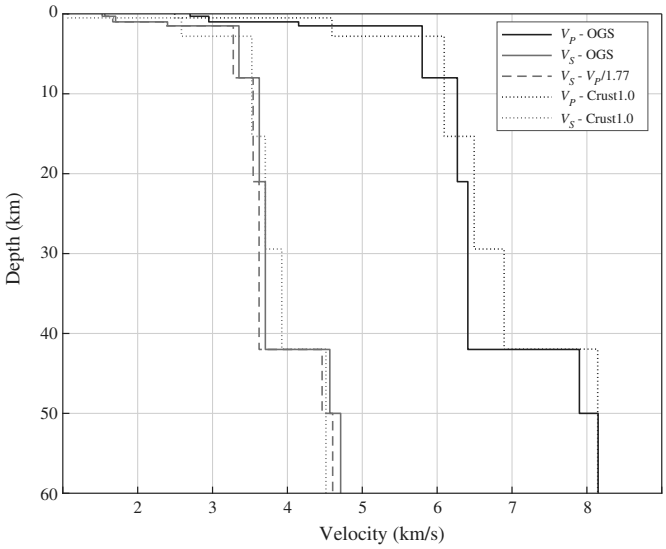

Figure 2. Reference velocity models of the study area. The velocity model from the OGS (Darold *et al.*, 2015) is denoted by solid lines, with the *S*-wave velocity on the left and the *P*-wave velocity on the right. The OGS velocity model assumes a constant V_P/V_S ratio of 1.73. Using a V_P/V_S ratio of 1.77 instead, we derive a new shear-wave velocity model, denoted by the dashed line. The velocity model from CRUST1.0 (Laske *et al.*, 2013) is shown by the dotted lines for comparison.

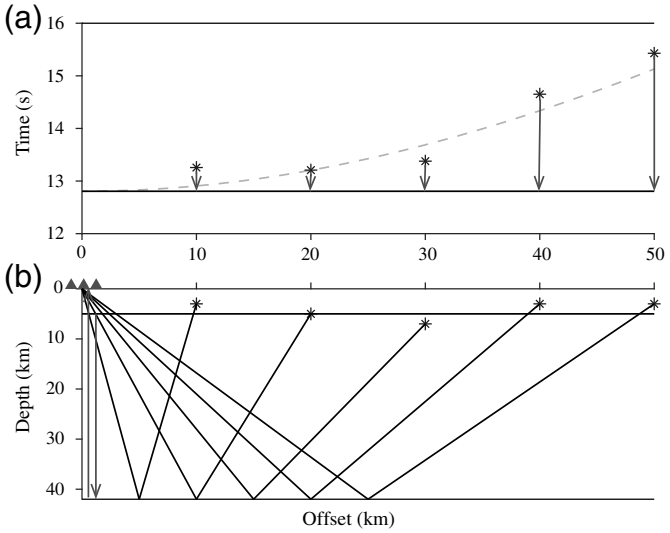

Figure 3. (a) Moveout corrections for the Moho reflections. The dashed line is the predicted Moho reflected arrival times for a reference 5 km depth source, from the OGS velocity model (Darold *et al.*, 2015). (b) A schematic diagram of the Moho reflected rays. The asterisks represent seismic events with different offsets and focal depths from the receiver array depicted by triangles. Moveout corrections are performed for each seismic event and receiver pair. The moveout time shifts flatten the Moho reflected arrivals and also correct for the event depths to a standard depth.

moveout corrections performed for the alignment of the Moho-reflected signals.

The dashed line in Figure 3a is a schematic of Moho reflected arrival times based on ray tracing for the OGS velocity model (Darold *et al.*, 2015) for a standard focal depth of 5 km. The predicted Moho reflection arrival times have offsets ranging from 0 to 50 km. The asterisks illustrate the Moho reflection arrival times for events of different focal depths reported in the OGS earthquake catalog. The offsets are calculated from the latitudes and longitudes of the receivers and OGS-located events. To account for event depth variability, each trace is shifted in time by a time difference between the predicted Moho reflection arrival times ray-traced for a 5 km depth source and the OGS reported event depths. Each trace is then moveout-corrected by the time between the dashed line and the flat line. In this way, the delay times resulting from offset are compensated for. The total time shift for each trace is denoted by the arrows in Figure 3a, integrating the time shifts for the variability in both event depth and offset. The Moho reflection arrival times are then approximately flattened for stacking along the receiver array for a given event.

Figure 3b illustrates the ray tracing for the Moho reflections. The asterisks and triangles represent seismic events and receiver array, respectively. The schematic ray paths are denoted by black lines between seismic events and receiver array. The moveout corrections then flatten the arrival times to the zero-offset time for a standard 5 km event depth. This then allows for stacking of the arrivals across the array for each event.

Stacking for Moho Reflections

Single-event stacking

We analyzed the later *P*- and *S*-wave arrivals for the receiver gathers from events within 50 km of the center of the array. Moveout corrections and receiver stacking were then applied to identify the Moho reflections on the vertical and horizontal transverse components. Corrections for the reported focal depths were applied to a standard depth of 5 km.

Figure 4 shows receiver gathers for two seismic events recorded on the vertical component by the east–west linear array nodal stations. Each trace is low-pass-filtered to 2 Hz and gained by a power of t to, approximately, equalize the amplitude decay with time. The solid and dashed lines are the predicted arrival times for the *P* and *PmP* phases from ray tracing, after a moveout correction for the *PmP* arrival time has been applied. The rightmost traces for each single event receiver gather are the moveout-corrected stacked traces. The arrows on the right denote the estimated arrival times of the *P*, *S*, and *PmP* on the stacked trace.

Figure 5 shows receiver gathers for two events recorded on the transverse component. Each trace is low-pass-filtered to 1.5 Hz and gained by a power of t to approximately equalize the amplitude decay with time. The solid and dashed lines are

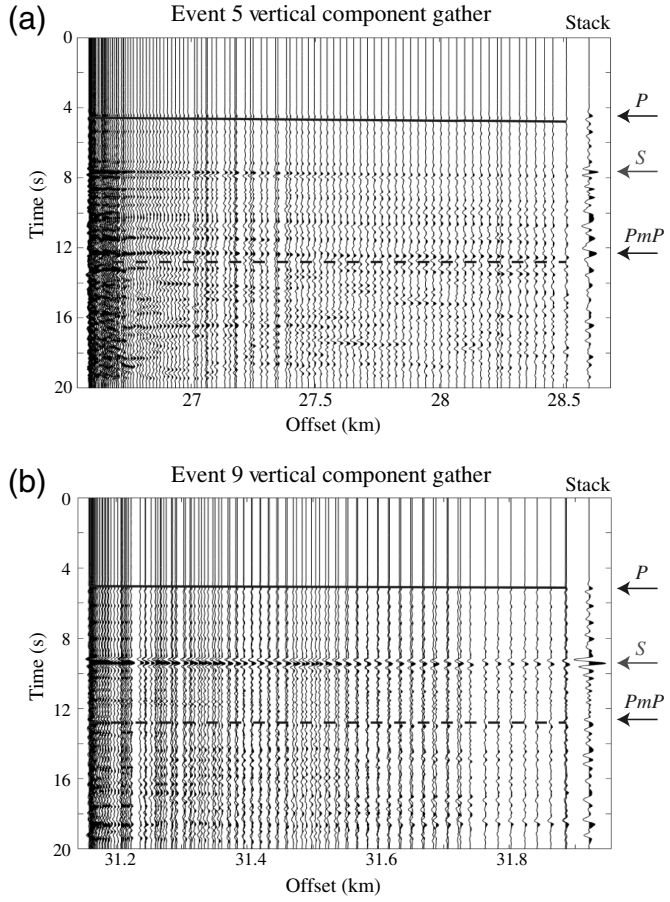

Figure 4. (a) A single-event receiver gather of the vertical components recorded by the east–west linear array nodal stations for event 5 in the supplemental material. Each trace is low-pass-filtered to 2 Hz and gained by a power of t to approximately equalize the amplitude decay with time. Solid and dashed lines are the predicted arrival times for the *P* and *PmP* from ray tracing, after a moveout correction for the *PmP* arrival. The rightmost trace is the event stack. Arrows on the right denote the observed arrival times of the *P*, *S*, and *PmP* on the stacked trace. (b) A similar plot for event 9.

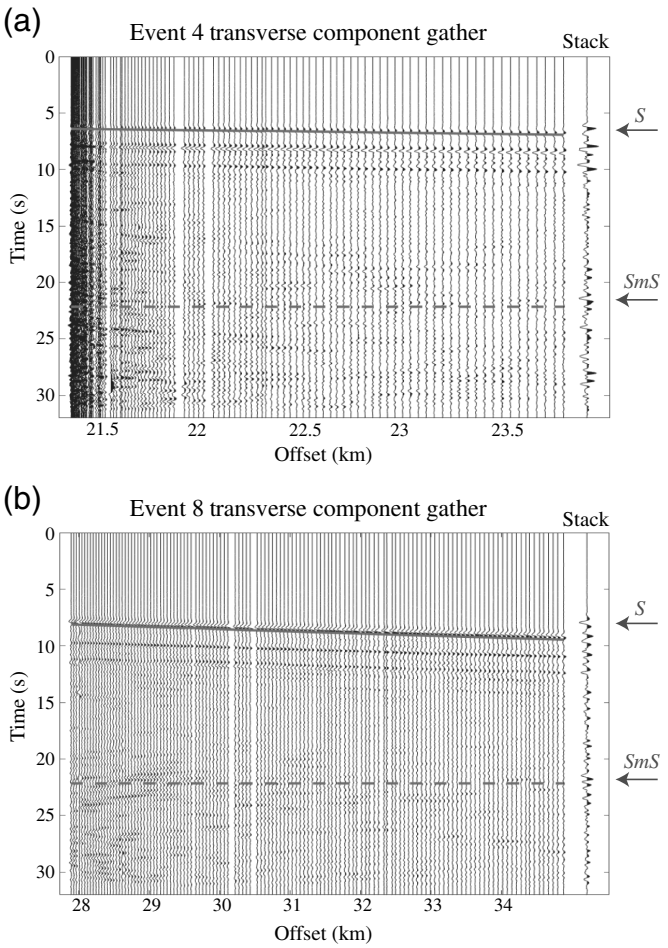

Figure 5. (a) A single-event receiver gather of the transverse component recorded by east–west linear array stations for event 4 in the supplemental material. Each trace is low-pass-filtered to 1.5 Hz and gained by a power of t to approximately equalize the amplitudes in time. Solid and dashed lines are the predicted *S* and *SmS* arrivals, after a moveout correction for the *SmS* arrival time. The rightmost trace in each single-event receiver gather is the stack. (b) A similar plot for event 8.

the predicted *S* and *SmS* arrivals, after a moveout correction for the predicted *SmS* phase. The rightmost traces in each single-event receiver gather are the moveout-corrected stacked traces. The arrows on the right denote the estimated arrival times of the *S* and *SmS* on the stacked trace.

The filtering, gaining, moveout corrections, and stacking are used to bring out the Moho reflected signals. The observed Moho reflection signals could arrive earlier or later than the predicted arrival times from the ray tracing. The deviation between observed and predicted Moho reflected arrival times could result from variations in Moho depths, location and focal depth variability in the OGS earthquake catalog and velocity variability.

Multiple-event stacking

To further enhance the Moho reflection signals, 17 seismic events within 50 km of the center of the array were selected based on signal-to-noise level and event size to perform multiple-event stacks for the *P*- and *S*-wave Moho reflections. We also looked for events with offsets from the array in which there was no interference between the Moho reflections and other phases. The selected pre-critical seismic events can be found in the supplemental material with distances less than 50 km from the array and are shown by the dark black dots in Figure 1.

Figure 6 illustrates the stacking of multiple events on the vertical component and the improvement of stacking by incorporating static and polarity corrections. Each trace on the left in Figure 6a is a single-event receiver gather stacking result. The rightmost trace is the multiple-event stacked trace. The line on top of each trace is the trace envelope. The Hilbert transform is used to form the analytic signal, which is a

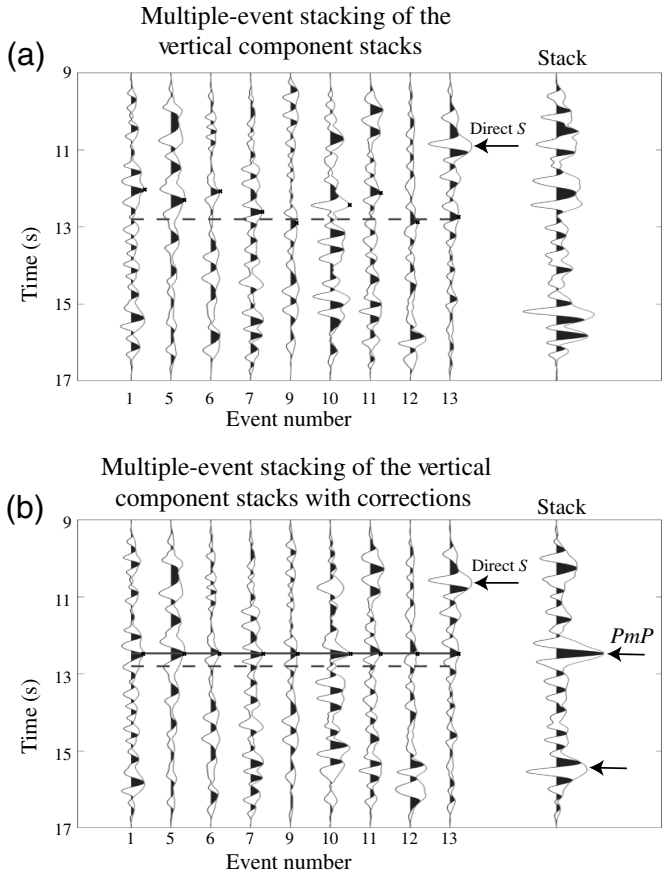

Figure 6. (a) Multiple-event stacking of the vertical-component stacks. Each trace on the left is a single-event receiver stack result. The rightmost trace is the multiple-event stacked trace. For each trace, the envelope is also shown. The dashed line is the predicted time of the normal-moveout-corrected predicted *PmP* arrivals for the OGS model. The direct *S* is also shown for one event. (b) The multiple-event stack of the vertical component after static and polarity corrections. The dashed line is the predicted moveout-corrected time of the *PmP* from the OGS model. The solid line is the average of the envelope peaks denoting the predicted Moho reflection time. The direct *S* wave is shown by arrows in both panels (a) and (b). Static corrections and polarity corrections are applied to the individual traces prior to stacking, with the stack shown on the right. The inferred *PmP* arrival is shown by an arrow. The lower arrow on the stack could be the location of the surface-reflected *sPmP* arrival.

complex time signal whose real part is the original signal and imaginary part is the Hilbert transform of the original signal (Shin and Hammond, 2008). The magnitude of analytical signal is the instantaneous amplitude that is the envelope of the original signal.

After the envelope is calculated, the local maximum of the envelope around the predicted Moho reflection, within ± 1.5 s of the predicted arrival time, is determined. The average of the observed Moho reflection arrival times is calculated, and each trace is shifted to align the peaks of the envelopes. The standard deviation about the average line is 0.29 s and could result from lateral variability of the velocities, variations in the Moho depth, and uncertainties in the event locations and depths.

Sign corrections of the waveforms were also applied at the peak of the envelopes. Traces with negative amplitudes at the peak of the envelopes are multiplied by a negative one to account for the variability of polarities, resulting from the event focal mechanisms, and possible effects from local structure. The corrected receiver stacked traces are then stacked in Figure 6b. The dashed line is the predicted moveout-corrected arrival times from the OGS model, and the solid line is the mean of the envelope peaks. The location of the direct *S* wave is shown by an arrow. After the static and polarity corrections, the stacked trace is shown on the rightmost trace. The estimated *PmP* is shown by the arrow. Also shown by the lower arrow on the stack in Figure 6b is the possible location of the surface-reflected *sPmP* arrival, although this is less evident on the individual event stacks.

Figure 7 shows a similar plot for the multiple-event stacking on the transverse component. The Moho reflection for the *S* wave can also be enhanced by the multiple-event stacking after similar static corrections and sign corrections for single-event receiver stacks, in which the inferred *SmS* is shown by the arrow. The lower arrow in Figure 7b is the possible arrival of the surface-reflected *sSmS* arrival; however, this is less evident on the individual event stacks.

The average absolute deviations about the average lines for the *PmP* and *SmS* arrivals are 0.29 and 0.40 s, respectively. The average standard errors for the selected events from the OGS catalog are 0.57 km for the horizontal locations and 1.1 km for the depths. For a 25 km offset and 5 km depth earthquake, the largest arrival-time deviations obtained from ray tracing for the errors in horizontal location and depth are 0.18 s for the *PmP* and 0.32 s for the *SmS*. These are comparable with the deviations about the average lines for the *PmP* and *SmS* arrivals, with additional components of the deviations resulting from lateral velocity variations and Moho depth.

The multiple-event stacks are used to identify the Moho reflections from the vertical *P* waves and transverse *S* waves. The zero-offset results from multiple-event stacks can then be used to estimate the average *P*- and S-wave velocity ratio, V_P/V_S, and the corresponding Poisson's ratio for the crust in this area. The normal-moveout-corrected *P*- and *S*-wave arrival times from the multiple-event stacks, after static and polarity sign corrections, are 12.57 and 22.28 s for *P* and *S* waves, respectively. The uncertainties for the stacked zero-offset Moho reflection arrival times are, approximately, 0.15 s on the stacked traces. This results in an average crustal V_P/V_S ratio of 1.77 ± 0.02 and a corresponding Poisson's ratio of 0.266 ± 0.009.

The OGS velocity model of Darold *et al.* (2015) used an assumed V_P/V_S ratio of 1.73. The velocity model from CRUST1.0 (Laske *et al.*, 2013) near the array has a variable V_P/V_S ratio with depth, with an average V_P/V_S for the crust

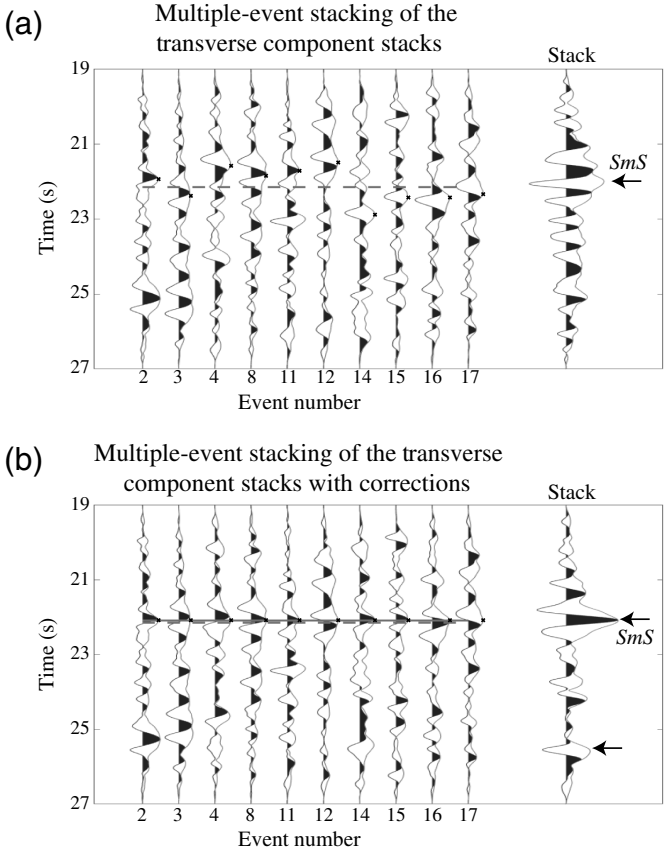

Figure 7. (a) Multiple-event stacking of the transverse component stacks. Each trace on the left is a single-event receiver stack result. The dashed line is the predicted time for the moveout corrected *SmS* from the OGS model. The rightmost trace is the multiple-event stacked trace. (b) The multiple-event stack of the transverse component after static and polarity corrections. Dashed line is the predicted time for the moveout corrected *SmS* from the OGS model. The solid line is the average of the envelope peaks denoting the inferred Moho reflection time. Static corrections and polarity corrections are applied to the individual traces prior to stacking, with the stack shown on the right. The inferred *SmS* arrival is shown by an arrow. The lower arrow on the stack could be the location of the surface-reflected *sSmS* arrival.

of 1.75. The average Poisson's ration for the continental crust has been estimated as 0.265 from rock sample measurements (Christensen, 1996). Also an early study by Zandt and Ammon (1995) estimated a Poisson's ratio of 0.27 for platform areas of the continental crust.

Receiver functions can be used to estimate the crustal V_P/V_S using the H – κ method (Zhu and Kanamori, 2000). From the EarthScope Automated Receiver Survey (EARS, Crotwell and Owens, 2005; IRIS, 2010), the V_P/V_S and Poisson's ratio are quite variable in the study area. Individual station values and a map of V_P/V_S values across the United States are given by IRIS (2010). Using the broadband stations from the IRIS Community Wavefield Experiment in Oklahoma, the V_P/V_S values range from 1.73 to 2.10, and Poisson's ratios range from 0.25 to 0.35. The V_P/V_S values from receiver functions, however, can have significant variability resulting from difficulties in the measurements of later arrivals of the receiver functions at specific stations. Based on results from well-log information, Schoenball and Ellsworth (2017) used a V_P/V_S of 1.78 to revise the OGS velocity model for their study. This is similar to the average crustal V_P/V_S of 1.77, found in this study, from the *PmP* and *SmS* arrivals. The modified V_S velocities assuming a V_P/V_S of 1.77 is shown by the dashed line in Figure 2.

Time-to-Depth Conversion

The multiple-event stacking results after corrections are used to perform the time-to-depth conversions. The Moho depth is shown for both *PmP* and *SmS*, after time-to-depth conversions in Figure 8. We use the OGS velocity model as a starting model and adjust the V_P/V_S ratio to make Moho depth from the *PmP* and *SmS* arrivals consistent. Deconvolutions are also performed on the multiple-event stacks to mitigate the effects of the later arrivals on the *PmP* and *SmS* traces.

Figure 8 shows the Moho reflection traces and their deconvolutions with both time and depth. Figure 8a shows the *PmP* and decon-*PmP* traces with time. The left trace is the multiple-event stack of the vertical component after static and polarity corrections. A tapering is applied between 9 and 11 s to mitigate the effect of direct *S* arrivals. Slight filtering is also applied to make the frequency content on the vertical component comparable to that of the transverse component. The right trace in Figure 8a is the deconvolution to remove the second pulse between 15 and 16 s. Assuming that the stacked trace $y(t)$ is comprised of the Moho reflection pulse $r(t)$ and a delayed pulse $a \cdot r(t-\tau)$, in which a is the amplitude of the second pulse and τ is the time delay of the second pulse, the stacked trace $y(t)$ can be approximated as

$$y(t) = r(t) + a \cdot r(t-\tau). \quad (1)$$

The corresponding Fourier transform can be written as

$$Y(\omega) = R(\omega)(1 + ae^{-i\omega\tau}). \quad (2)$$

In which ω is the radial frequency. The Fourier transform of $r(t)$, that is $R(\omega)$, can then be deconvolved as

$$R(\omega) = \frac{(1 + ae^{i\omega\tau})Y(\omega)}{(1 + ae^{i\omega\tau})(1 + ae^{-i\omega\tau}) + \varepsilon^2}, \quad (3)$$

in which ε is a small damping parameter used to stabilize the deconvolution.

Figure 8b shows the *SmS* and decon-*SmS* traces with time. The left trace is the multiple-event stack of the transverse component after static and polarity corrections. The right trace in

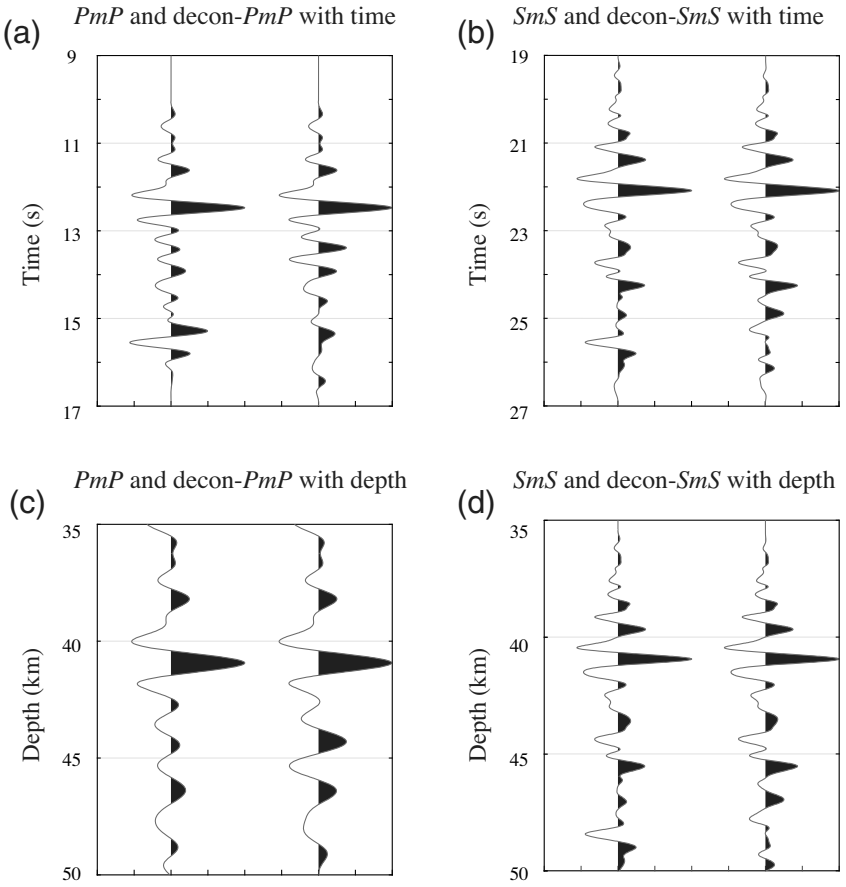

Figure 8. (a) *PmP* and decon-*PmP* traces with time. The left trace is the multiple-event stack of the vertical component after static and polarity corrections. A tapering is applied between 9 and 11 s to mitigate the effect of direct *S* arrivals. Slight filtering is also applied to make the frequency content on the vertical component comparable with that of the transverse component. The right trace is the deconvolution of the left trace to remove the later pulse between 15 and 16 s. (b) *SmS* and decon-*SmS* traces with time. The left trace is the multiple-event stack of the transverse component after static and polarity corrections. The right trace is the deconvolution of the left trace to remove the later pulse between 25 and 26 s. (c) *PmP* and decon-*PmP* traces with depth. The OGS *P*-wave velocity model is used to perform the time-to-depth conversion. The Moho depth obtained for the *P*-wave Moho reflection is at 41 km. (d) *SmS* and decon-*SmS* traces with depth. The *S*-wave velocity calculated from OGS *P*-wave velocity using a V_P/V_S ratio of 1.77 is used to perform the time-to-depth conversion. The Moho depth obtained from the *S*-wave Moho reflection is also at 41 km consistent with the estimate from the *PmP* traces with depth.

Figure 8b is deconvolution to remove the second pulse between 25 and 26 s, in a similar fashion as for the *PmP*.

Figure 8c shows the *PmP* and decon-*PmP* traces with depth. The OGS *P*-wave velocity model is used to perform a time-to-depth conversion, in which, for each point of the time axis, an equivalent depth is found by ray tracing for a source with a 5 km focal depth, assuming single scattering from reflectors at depth. The Moho depth calculated from the *P*-wave Moho reflection is 41 ± 0.6 km, in which the uncertainty is based on the width of the central pulse of the *PmP* arrival converted to depth. This is slightly shallower than the 42 km Moho depth from the original OGS velocity model.

Figure 8d shows the *SmS* and decon-*SmS* traces with depth. The Moho depth is converted from time in a similar fashion as for the *P*-wave traces and is dependent on the V_S velocity model used. The original OGS velocity model assumed a V_P/V_S ratio of 1.73, but this does not result in a consistent Moho depth estimation between the *PmP* and *SmS* traces converted to depth. However, using a V_P/V_S ratio of 1.77 to convert the *SmS* trace to depth results in a consistent Moho depth estimation with the *PmP* trace. Converting from time to depth results in a better resolution in depth for the *S*-wave traces, compared with the *P*-wave traces.

There are two possibilities for the second arrivals on the *PmP* and *SmS* traces that arrive later than the Moho reflections, between 9 and 11 s on the *PmP* trace in time on the left plot of Figure 8a and between 25 and 26 s on the *SmS* trace in time on the left plot of Figure 8b, respectively. The first possibility is that these are primary reflections from a deeper interface. As shown in the OGS velocity model in Figure 2, there could be a potential deeper interface at around 50 km in this model.

The left traces in Figure 8c,d are the time-to-depth conversion of the multiple-event stacks on the vertical and transverse components. The depth range on these plots is shown from 35 to 50 km. If the later second pulses are primary reflections from a deeper interface, this interface will be deeper than 50 km, as shown in Figure 8c, for the *P*-wave converted to depth and at 48 km, in Figure 8d, for the *S*-wave converted to depth. The depth of a possible deeper interface for these later phases is thus inconsistent between the *P*-wave and *S*-wave traces converted to depth. We, therefore, exclude the possibility that these later arrivals result from a deeper interface.

The second possibility is that the later phases are surface-reflected phases. However, to be consistent between the *PmP*

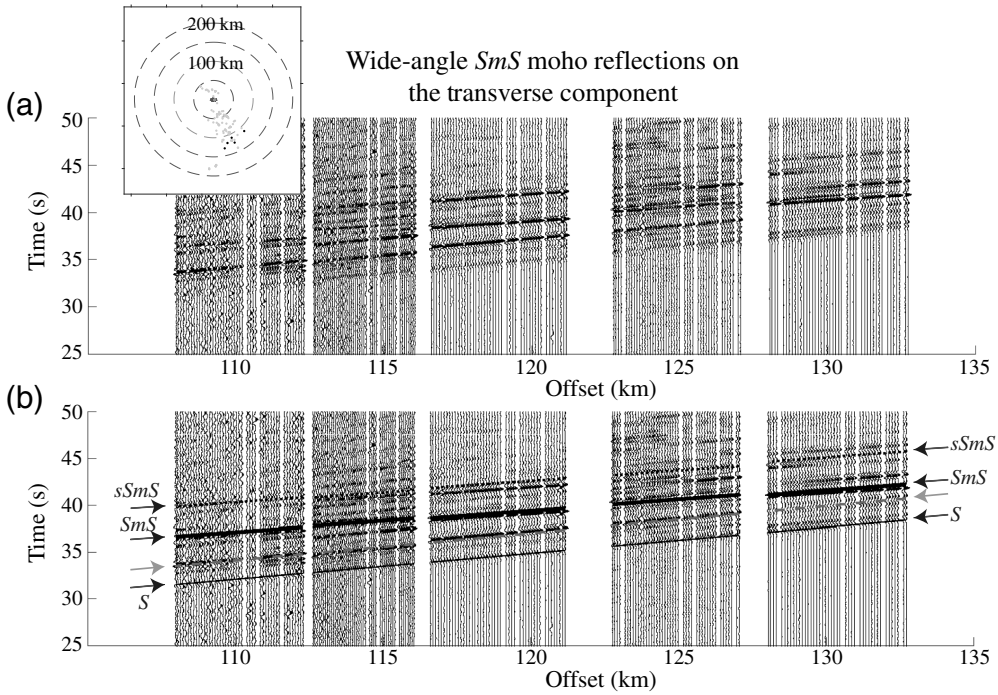

Figure 9. (a) Composite record section of the wide-angle *SmS* Moho reflections on the transverse component, recorded on the left north–south linear nodal array stations. Each trace is low-pass-filtered to 1.5 Hz. The inset map shows the location of earthquakes, denoted by gray dots. The black dots are selected for the plot. (b) Composite record section with identified phase shown. Thick solid line and arrows show the predicted *SmS* arrival. The arrival times are ray-traced from the modified OGS model and the depths in the OGS seismic catalog. Thin solid line and arrows show the direct *S* arrival. The surface-reflected Moho reflection phase *sSmS* is also denoted by the dotted line and arrows. Light-gray dashed line and arrow show either a surface-reflected direct wave *sS* or a surface wave with a 3.45 km/s apparent velocity in a narrow frequency band.

and *SmS* traces, the later pulse on the *PmP* trace would need to be an *sPmP* arrival and the later phase on the *SmS* trace an *sSmS* arrival. For zero-offset propagation, the amplitude for the *S*-to-*P* conversion at the free surface would be zero. However, the stacked *P*-wave trace is derived from the stacking of traces with nonzero offsets, and this would allow for a nonzero amplitude on the stacked equivalent zero-offset *P*-wave trace. Also, for earthquake sources the *S*-wave amplitudes would be approximately (V_P/V_S)^3 or 5.5 times larger in amplitude than the *P* waves from the source, assuming a $V_P/V_S = 1.77$ (Aki and Richards, 2002). The later arrival on the *P*-wave trace is, however, still about 0.2 s later than would be fully consistent with an *sSmS*on the *S*-wave trace. However, this could result from some phase distortion from the processing for the second arrival on the *P*-wave trace. If the later arrivals are surface-reflected arrivals, the traces on the right for each of the subplots in Figure 8 would show the results for just the primary reflection arrivals, with the later arrivals removed by deconvolution.

Further sources of errors in the results would be from the assumed velocity model. For the analysis performed here, the velocity model in the vicinity of the array is assumed to be laterally homogeneous, and static corrections are implemented to account for small lateral inhomogeneities. For a variation of the velocity model in depth, this would affect the *P*-wave and *S*-wave results in a similar fashion, in terms of the inferred average crustal V_P/V_S ratio. However, a slightly faster lower crust than that of the assumed OGS velocity model, as inferred, for example, by Ratre and Behm (2019), would make the estimates of Moho depths correspondingly deeper.

Wide-Angle Moho Reflections

As an illustration of recording wide-angle reflections from the Moho for a large-*N* array, several seismic events were selected to form composite record sections. The selection of these seismic events was based on several criteria, including background cultural noise level and the magnitude of seismic events. Selected events for the analysis of wide-angle arrivals, with distances between 90 and 135 km from the center of the array, are listed in the supplemental material.

The transverse *S*-wave components from five seismic events recorded on the left north–south linear nodal array stations are plotted on the composite record section in Figure 9a. The events are 21, 22, 24, 25, and 26 in the supplemental material. Each trace is low-pass filtered to 1.5 Hz. Figure 9b shows the annotations of several observed seismic phases. The thick solid line and arrows show the predicted *SmS* arrival, in which the arrival times are ray-traced from the modified OGS velocity model and the depths in the OGS seismic catalog. A Moho depth of 40 ± 1 km was inferred for the wide-angle modeling of these events, with epicenter-to-station distances of 100–135 km from the array for the *S* phases. However, due to the depth variability in the catalog, the predicted arrival times may deviate from the observed arrival times. The thin solid line and arrows show the direct *S* arrival, which is the first strong seismic phase on the transverse component. The light gray dashed line and arrows show the location of an arrival after the direct *S* but followed by the *SmS* arrival from the Moho at this distance range, which could be a surface-reflected direct arrival *sS* or a surface wave with an apparent speed of

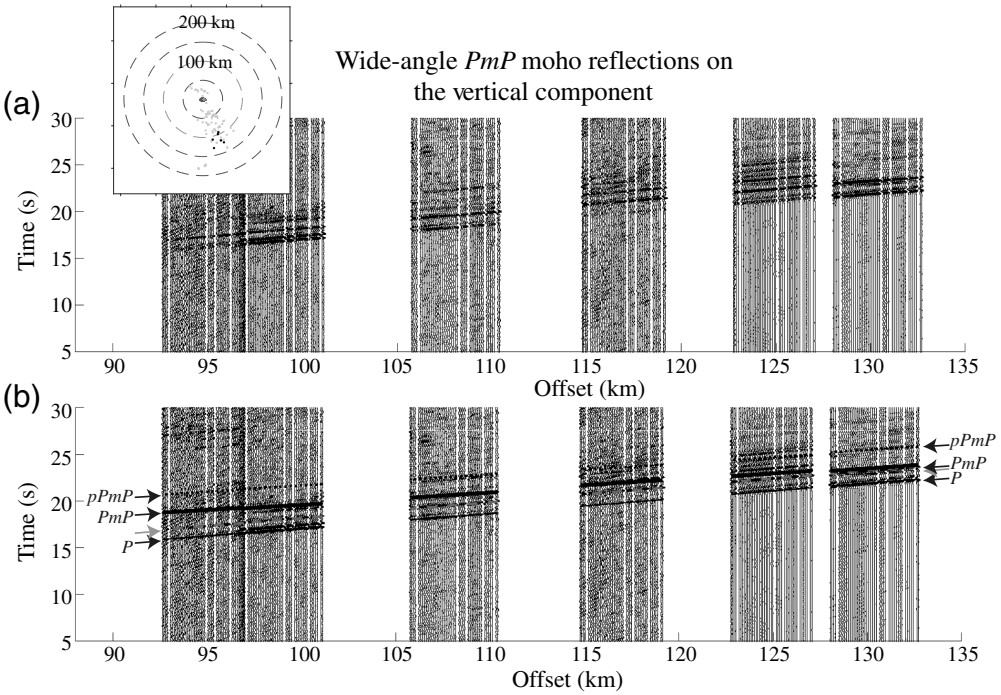

Figure 10. (a) Composite record section of the wide-angle *PmP* Moho reflections on the vertical component, recorded on the left north–south linear nodal array stations. Each trace is low-pass-filtered to 2 Hz. The inset map shows the location of earthquakes, denoted by gray dots. The black dots are selected for the analysis. (b) Composite record section with identified phase shown. Thick solid line and arrows show the predicted *PmP* arrival. The arrival times are ray-traced from the modified OGS velocity model and the depth in the OGS seismic catalog. The thin solid line and arrows show the direct *P* arrival. The surface-reflected Moho reflection phase *pPmP* is also denoted by the dotted line and arrows. Light-gray dashed line and arrows show a possible surface-reflected direct wave *pP*.

3.45 km/s in a narrow band frequency of 0–1.5 Hz (Zhan *et al.*, 2010). The surface-reflected Moho reflection phase *sSmS* is also denoted by the solid dashed line and arrows in Figure 9b. The amplitude of this phase varies between events, partly due to the shallow subsurface structure on the source side.

The vertical *P*-wave components from six selected seismic events recorded on the left north–south linear nodal array stations are plotted on the composite record section in Figure 10a. The events are 18, 19, 20, 23, 25 and 26 in the supplemental material. Each trace is low-pass filtered to 2 Hz. Figure 10b shows the annotations of several observed seismic phases. The thick solid line and arrows show the predicted *PmP* arrival, in which the arrival times are ray-traced from the modified OGS velocity model and the depth in the OGS seismic catalog. Again, a Moho depth of 40 ± 1 km was inferred for the wide-angle modeling of these events with epicenter-to-station distances of 90–135 km from the array for the *P* phases. The thin solid line and arrows show the direct *P* arrivals. The slight-gray dashed line and arrows show the location of an arrival after the direct *P* but followed by the *PmP* arrival from the Moho, which could be the surface-reflected directed arrival *pP*. The surface-reflected Moho reflection phase *pPmP* is also denoted by the dotted line and arrows in Figure 10b. Due to the smaller energy of *P* wave from earthquakes and the affects from *SV* waves on the vertical component, the *PmP* Moho reflections are less evident than the *SmS* Moho reflections. The difference between the pre-critical and wide-angle Moho depth estimates could result from some lateral variability between the seismic array and the more distant wide-angle events. However, both estimates are shallower than the original OGS model, and this could also result from a somewhat faster lower crust.

Conclusions

The deployments of large-*N* seismic arrays have become increasingly popular, enabling advances in subsurface imaging. In this study, the *P*- and *S*-wave later arrivals from local seismic events near the large-*N* IRIS Community Wavefield Experiment in Oklahoma are used to illustrate the analysis of Moho reflections and average crustal thickness and V_P/V_S ratio near the array. The pre-critical *PmP* and *SmS* Moho reflections for events within 50 km of the center of the array were first found on single-event stacks, by applying normal moveout corrections, low-pass filtering and gaining methods. Multiple-event stacks were then applied to further enhance the Moho reflection signals from the stacking of the single-event receiver gathers. Static corrections and polarity corrections were applied to account for lateral variability of Moho depth and velocity structure, and uncertainties in the event locations and focal depths. The arrival times of the *PmP* and *SmS* on multiple-event stacked traces after normal-moveout, static, and polarity corrections were used to estimate an average crustal V_P/V_S ratio of 1.77 ± 0.02, with a Poisson's ratio of 0.266 ± 0.009 near the array. The inferred crustal V_P/V_S and Poisson's ratio are in good agreement with the previous studies for the average continental crust, although the results in the study area from receiver functions are more variable. Using a modified OGS velocity model with this Poisson's ratio, the time-to-depth converted *PmP* and *SmS* arrivals resulted in a Moho depth of 41 ± 0.6 km, which is slightly shallower than the 42 km for the original OGS model.

For selected events at epicenter-to-station distances of 90–135 km, the modeling of wide-angle arrivals provided additional constraints, and a Moho depth of 40 ± 1 km was inferred. The difference between the precritical and wide-angle Moho depth estimates could result from some lateral variability between the seismic array and the more distant wide-angle events as well as event depth uncertainties. However, both estimates are slightly shallower than the original OGS model, and this could also result from a somewhat faster lower crust.

This study shows that local seismic events, including induced events in areas with less natural background seismicity, can be used estimate properties and structure of the crust, which can then be used to better understand the tectonics of a given region. The recording of local seismicity on large-*N* arrays provides increased lateral phase coherence, and this allows for better identification of both precritical and wide-angle reflected arrivals.

Data and Resources

The seismic waveform data used in this study were collected as part of the Incorporated Research Institutions for Seismology (IRIS) Community Wavefield Experiment in Oklahoma. Data can be obtained from the IRIS Data Management Center at www.iris.edu. Supplemental material for this article includes a list of the seismic events used for this study. The hypocenter data for the events are from the Oklahoma Geological Survey at http://wichita.ogs.ou.edu/eq/catalog/2016/2016.csv. MATLAB software was used for the visualization, and several codes were modified from the CREWES MATLAB toolbox of the Consortium for Research in Elastic Wave Exploration Seismology, University of Calgary, Calgary, Alberta, Canada. All websites were last accessed in February 2020.

Acknowledgments

The authors thank the two anonymous Reviewers, the Associate Editor Dan McNamara, and the Editor for their constructive reviews, which substantially improved the article. The study was partially supported by U.S. National Science Foundation Grant EAR-1839322 and a Purdue Earth, Atmospheric, and Planetary Sciences (EAPS) travel grant for the first author.

References

Aki, K., and P. G. Richards (2002). *Quantitative Seismology*, University Science Books, Sausalito, California.

Anderson, K., J. Sweet, and B. Woodward (2016). IRIS community wavefield experiment in Oklahoma, Incorporated Research Institutions for Seismology, Other/Seismic Network, doi: 10.7914/SN/YW_2016.

Brenguier, F., P. Kowalski, N. Ackerley, N. Nakata, P. Boué, M. Campillo, E. Larose, S. Rambaud, C. Pequegnat, T. Lecocq, *et al.* (2016). Toward 4D noise-based seismic probing of volcanoes: Perspectives from a large-N experiment on Piton de la Fournaise Volcano, *Seismol. Res. Lett.* **87,** no. 1, 15–25, doi: 10.1785/0220150173.

Carbonell, R., A. Levander, and R. Kind (2013). The Mohorovičić discontinuity beneath the continental crust: An overview of seismic constraints, *Tectonophysics* **609,** 353–376, doi: 10.1016/j.tecto.2013.08.037.

Christensen, N. I. (1996). Poisson's ratio and crustal seismology, *J. Geophys. Res.* **101,** no. B2, 3139–3156, doi: 10.1029/95JB03446.

Cook, F. A., D. J. White, A. G. Jones, D. W. S. Eaton, J. Hall, and R. M. Clowes (2010). How the crust meets the mantle: Lithoprobe perspectives on the Mohorovičić discontinuity and crust–mantle transition, in special issue on the theme Lithoprobe – Parameters, processes, and the evolution, *Can. J. Earth Sci.* **47,** no. 4, 315–351, doi: 10.1139/E09-076.

Crotwell, H. P., and T. J. Owens (2005). Automated receiver function processing, *Seismol. Res. Lett.* **76,** no. 6, 702–709, doi: 10.1785/gssrl.76.6.702.

Darold, A. P., A. A. Holland, J. K. Morris, and A. R. Gibson (2015). *Oklahoma earthquake summary report 2014*, *Okla. Geol. Surv. Open-File Rept. OF1-2015*, 1–46.

Eddy, A. C., and S. H. Harder (2018). Correlation of local earthquakes to form a reflection image beneath the IRIS Community Wavefield Experiment, Grant County, Oklahoma, *American Geophysical Union (AGU) Fall Annual Meeting*, Washington DC, 10–14 December 2018.

Ellsworth, W. L. (2013). Injection-induced earthquakes, *Science* **341,** no. 6142, 1225942, doi: 10.1126/science.1225942.

Evanzia, D., J. Pulliam, R. Ainsworth, H. Gurrola, and K. Pratt (2014). Seismic Vp & Vs tomography of Texas & Oklahoma with a focus on the Gulf Coast margin, *Earth Planet. Sci. Lett.* **402,** 148–156, doi: 10.1016/j.epsl.2013.12.027.

Fan, W., and J. J. McGuire (2018). Investigating microearthquake finite source attributes with IRIS Community Wavefield Demonstration Experiment in Oklahoma, *Geophys. J. Int.* **214,** no. 2, 1072–1087, doi: 10.1093/gji/ggy203.

Freed, D. (2008). Cable-free nodes: The next generation land seismic system, *The Leading Edge* **27,** no. 7, 878–881, doi: 10.1190/1.2954027.

Glasgow, M. E., B. Schmandt, and S. M. Hansen (2018). Upper crustal low-frequency seismicity at Mount St. Helens detected with a dense geophone array, *J. Volcanol. Geotherm. Res.* **358,** 329–341, doi: 10.1016/j.jvolgeores.2018.06.006.

Griffin, J. D., R. L. Nowack, W. P. Chen, and T. L. Tseng (2011). Velocity structure of the Tibetan lithosphere: Constraints from P-wave travel-times of regional earthquakes, *Bull. Seismol. Soc. Am.* **101,** no. 4, 1938–1947, doi: 10.1785/0120100229.

Hansen, S. M., and B. Schmandt (2015). Automated detection and location of microseismicity at Mount St. Helens with a large-N geophone array, *Geophys. Res. Lett.* **42,** no. 18, 7390–7397, doi: 10.1002/2015GL064848.

Hansen, S. M., B. Schmandt, A. Levander, E. Kiser, J. E. Vidale, G. A. Abers, and K. C. Creager (2016). Seismic evidence for a cold serpentinized mantle wedge beneath Mount St Helens, *Nat. Commun.* **7,** no. 1, 13,242, doi: 10.1038/ncomms13242.

Hillers, G., P. Roux, M. Campillo, and Y. Ben-Zion (2016). Focal spot imaging based on zero lag cross-correlation amplitude fields: Application to dense array data at the San Jacinto fault zone, *J. Geophys. Res.* **121,** no. 11, 8048–8067, doi: 10.1002/2016JB013014.

Hincks, T., W. Aspinall, R. Cooke, and T. Gernon (2018). Oklahoma's induced seismicity strongly linked to wastewater injection depth, *Science* **359,** no. 6381, 1251–1255, doi: 10.1126/science.aap7911.

Inamori, T., S. Horiuchi, and A. Hasegawa (1992). Location of mid-crustal reflectors, by a reflection method using aftershock waveform data in the focal area of the 1984 Western Nagano Prefecture earthquake, *J. Phys. Earth* **40,** 379–393.

Incorporated Research Institutions for Seismology (IRIS), DMC (2010). Data services products: EarthScope Automated Receiver Survey (EARS), doi: 10.17611/DP/EARS.1.

Johnson, K. S. (2008). Geologic history of Oklahoma, *Earth sciences and mineral resources of Oklahoma: Oklahoma Geological Survey, Educational Publication* 9**,** 3–5.

Karplus, M., and B. Schmandt (2018). Preface to the focus section on geophone array seismology, *Seismol. Res. Lett.* **89,** no. 5, 1597–1600, doi: 10.1785/0220180212.

Keranen, K. M., M. Weingarten, G. A. Abers, B. A. Bekins, and S. Ge (2014). Sharp increase in central Oklahoma seismicity since 2008 induced by massive wastewater injection, *Science* **345,** no. 6195, 448–451, doi: 10.1126/science.1255802.

Kiser, E., A. Levander, C. Zelt, B. Schmandt, and S. Hansen (2019). Upper crustal structure and magmatism in southwest Washington: V_p, V_s, and V_p/V_s results from the iMUSH active-source seismic experiment, *J. Geophys. Res.* **124,** no. 7, 7067–7080, doi: 10.1029/2018JB016203.

Kiser, E., I. Palomeras, A. Levander, C. Zelt, S. Harder, B. Schmandt, S. Hansen, K. Creager, and C. Ulberg (2016). Magma reservoirs from the upper crust to the Moho inferred from high-resolution Vp and Vs models beneath Mount St. Helens, Washington State, USA, *Geology* **44,** no. 6, 411–414, doi: 10.1130/G37591.1.

Langenbruch, C., and M. D. Zoback (2016). How will induced seismicity in Oklahoma respond to decreased saltwater injection rates? *Sci. Adv.* **2,** no. 11, e1601542 , doi: 10.1126/sciadv.1601542.

Laske, G., G. Masters, Z. Ma, and M. Pasyanos (2013). Update on CRUST1.0—A 1-degree global model of Earth's crust, *Geophys. Res. Abstr.* 15**,** Abstract EGU2013-2658, 2013.

Levander, A., and G. Nolet (Editors) (2005). *Seismic Earth: Array Analysis of Broadband Seismograms*, Geophysical Monograph Series, Vol. 157, American Geophysical Union, Washington, DC, 252 pp.

Li, C., Z. Li, Z. Peng, C. Zhang, N. Nakata, and T. Sickbert (2018). Long-period long-duration events detected by the IRIS Community Wavefield demonstration experiment in Oklahoma: Tremor or train signals? *Seismol. Res. Lett.* **89,** no. 5, 1652–1659, doi: 10.1785/0220180081.

Li, Z., Z. Peng, D. Hollis, L. Zhu, and J. McClellan (2018). High-resolution seismic event detection using local similarity for large-N arrays, *Sci. Rep.* **8,** no. 1, 1646, doi: 10.1038/s41598-018-19728-w.

Lin, F.-C., D. Li, R. W. Clayton, and D. Hollis (2013). High-resolution 3D shallow crustal structure in Long Beach, California: Application of ambient noise tomography on a dense seismic array, *Geophysics* **78,** no. 4, Q45–Q56, doi: 10.1190/geo2012-0453.1.

Marsh, S. (2018). Development of a state-wide velocity profile in Oklahoma using ambient noise seismic tomography, *M.S. Thesis*, University of Oklahoma, Norman.

Mechie, J., W. Zhao, M. S. Karplus, Z. Wu, R. Meissner, D. Shi, S. L. Klemperer, H. Su, R. Kind, G. Xue, *et al.* (2012). Crustal shear (S) velocity and Poisson's ratio structure along the INDEPTH IV profile in northeast Tibet as derived from wide-angle data, *Geophys. J. Int.* **191,** 369–384, doi: 10.1111/j.1365-246X.2012.05616.1.

Mori, J., and D. Helmberger (1996). Large-amplitude Moho reflections (*SmS*) from Landers aftershocks, Southern California, *Bull. Seismol. Soc. Am.* **86,** no. 6, 1845–1852.

Nakata, N., J. P. Chang, J. F. Lawrence, and P. Boué (2015). Body wave extraction and tomography at Long Beach, California, with ambient-noise interferometry, *J. Geophys. Res.* **120,** no. 2, 1159–1173, doi: 10.1002/2015JB011870.

Nishitsuji, Y., E. Ruigrok, M. Gomez, K. Wapenaar, and D. Draganov (2016). Reflection imaging of aseismic zones of the Nazca slab by global-phase seismic interferometry, *Interpretation* **4,** no. 3, SJ1–SJ16, doi: 10.1190/INT-2015-0225.1.

Nowack, R. L., W.-P. Chen, and T.-L. Tseng (2010). Application of Gaussian-beam migration to multiscale imaging of the lithosphere beneath the Hi-CLIMB array in Tibet, *Bull. Seismol. Soc. Am.* **100,** no. 4, 1743–1754, doi: 10.1785/0120090207.

Oklahoma Geological Survey (OGS) Earthquake Catalog (2016). Available at http://wichita.ogs.ou.edu/eq/catalog/2016/2016.csv (last accessed February 2020).

Pei, S., Z. Peng, and X. Chen (2018). Locations of injection-induced earthquakes in Oklahoma controlled by crustal structures, *J. Geophys. Res.* **123,** 2332–2344, doi: 10.1002/2017JB014983.

Prodehl, C., and W. D. Mooney (2012). *Exploring the Earth's Crust—History and Results of Controlled-Source Seismology*, Geol. Soc. Am. Memoirs, Vol. 208, The Geological Society of America, Boulder, CO, 764 pp.

Qin, L., Y. Ben-Zion, H. Qiu, P.-E. Share, Z. E. Ross, and F. L. Vernon (2018). Internal structure of the San Jacinto fault zone in the trifurcation area southeast of Anza, California, from data of dense seismic arrays, *Geophys. J. Int.* **213,** no. 1, 98–114, doi: 10.1093/gji/ggx540.

Quiros, D. A., L. D. Brown, K. K. Davenport, J. A. Hole, A. Cabolova, C. Chen, L. Han, M. C. Chapman, and W. D. Mooney (2017). Reflection imaging with earthquake sources and dense arrays, *J. Geophys. Res.* **122,** 3076–3098, doi: 10.1002/2016JB013677.

Ratre, P., and M. Behm (2019). A comprehensive seismic 3D model of the central Oklahoma crust from local earthquake waveforms: implications for the mid-continent rift (MCR), *American Geophysical Union (AGU) Fall Annual Meeting*, San Francisco, California, 9–13 December 2019.

Riahi, N., and P. Gerstoft (2015). The seismic traffic footprint: Tracking trains, aircraft, and cars seismically, *Geophys. Res. Lett.* **42,** no. 8, 2674–2681, doi: 10.1002/2015GL063558.

Ringler, A. T., R. E. Anthony, M. S. Karplus, A. A. Holland, and D. C. Wilson (2018). Laboratory tests of three Z-land fairfield nodal 5-Hz, three-component sensors, *Seismol. Res. Lett.* **89,** no. 5, 1601–1608, doi: 10.1785/0220170236.

Rondenay, S. (2009). Upper mantle imaging with array recordings of converted and scattered teleseismic waves, *Surv. Geophys.* **30,** nos. 4/5, 377–405, doi: 10.1007/s10712-009-9071-5.

Roux, P., L. Moreau, A. Lecointre, G. Hillers, M. Campillo, Y. Ben-Zion, D. Zigone, and F. Vernon (2016). A methodological approach towards high-resolution surface wave imaging of the San Jacinto Fault Zone using ambient-noise recordings at a spatially dense array, *Geophys. J. Int.* **206,** no. 2, 980–992, doi: 10.1093/gji/ggw193.

Ruigrok, E., and K. Wapenaar (2012). Global-phase seismic interferometry unveils P-wave reflectivity below the Himalayas and Tibet,

Geophys. Res. Lett. **39,** no. 11, L11303, doi: 10.1029/2012GL051672.

Schmandt, B., and R. W. Clayton (2013). Analysis of teleseismic P waves with a 5200-station array in Long Beach, California: Evidence for an abrupt boundary to inner borderland rifting, *J. Geophys. Res.* **118,** no. 10, 5320–5338, doi: 10.1002/jgrb.50370.

Schoenball, J., and W. L. Ellsworth (2017). Waveform-relocated earthquake catalog for Oklahoma and Southern Kansas illumnitate the regional fault network, *Seismol. Res. Lett.* **88,** 1252–1258, doi: 10.1785/0220170083.

Shen, W., and M. H. Ritzwoller (2016). Crustal and uppermost mantle structure beneath the United States, *J. Geophys. Res.* **121,** 4306–4342, doi: 10.1002/2016JB012887.

Shin, K., and J. Hammond (2008). *Fundamentals of Signal Processing for Sound and Vibration Engineers*, John Wiley & Sons, Hoboken, New Jersey, 90–93.

Skoumal, R. J., J. O. Kaven, and J. I. Walter (2019). Characterizing seismogenic fault structures in Oklahoma using a relocated template-matching catalog, *Seismol. Res. Lett.* **90,** 1535–1540, doi: 10.1785/0220190045.

Sweet, J. R., K. R. Anderson, S. Bilek, M. Brudzinski, X. Chen, H. DeShon, C. Hayward, M. Karplus, K. Keranen, C. Langston, *et al.* (2018). A community experiment to record the full seismic wavefield in Oklahoma, *Seismol. Res. Lett.* **89,** no. 5, 1923–1930, doi: 10.1785/0220180079.

Thompson, D. A., N. Rawlinson, and H. Tkalčić (2019). Testing the limits of virtual deep seismic sounding via new crustal thickness estimates of the Australian continent, *Geophys. J. Int.* **218,** no. 2, 787–800, doi: 10.1093/gji/ggz191.

Tseng, T.-L., W.-P. Chen, and R. L. Nowack (2009). Northward thinning of Tibetan crust revealed by virtual seismic profiles, *Geophys. Res. Lett.* **36,** no. 24, L24304, doi: 10.1029/2009GL040457.

Walsh, F. R., and M. D. Zoback (2015). Oklahoma's recent earthquakes and saltwater disposal, *Sci. Adv.* **1,** no. 5, e1500195, doi: 10.1126/sciadv.1500195.

Walter, J. I., P. Ogwari, A. Thiel, F. Ferrer, *et al.* (2020). The Oklahoma Geological Survey statewide seismic network, *Seismol. Res. Lett.* **91,** no. 2A, 611–621, doi: 10.1785/0220190211.

Wang, H., D. Zhao, Z. Huang, M. Xu, L. Wang, Y. Nishizono, and H. Inakura (2018). Crustal tomography of the 2016 Kumamoto earthquake area in West Japan using *P* and *PmP* data, *Geophys. J. Int.* **214,** no. 2, 1151–1163, doi: 10.1093/gji/ggy177.

Wang, Y., A. Allam, and F. Lin (2019). Imaging the fault damage zone of the San Jacinto Fault near Anza with ambient noise tomography using a dense nodal array, *Geophys. Res. Lett.* **46,** no. 22, 12,938–12,948, doi: 10.1029/2019GL084835.

Wang, Y., F.-C. Lin, B. Schmandt, and J. Farrell (2017). Ambient noise tomography across Mount St. Helens using a dense seismic array, *J. Geophys. Res.* **122,** no. 6, 4492–4508, doi: 10.1002/2016JB013769.

Wang, Z., P. Persaud, and M. Behm (2019). Investigation of the crust in Oklahoma from broadband teleseismic receiver function, *American Geophysical Union (AGU) Fall Annual Meeting*, 9–13 December 2019, San Francisco, California.

Ward, K. M., and F. Lin (2017). On the viability of using autonomous three-component nodal geophones to calculate teleseismic Ps receiver functions with an application to Old Faithful, Yellowstone, *Seismol. Res. Lett.* **88,** no. 5, 1268–1278, doi: 10.1785/0220170051.

Weingarten, M., S. Ge, J. W. Godt, B. A. Bekins, and J. L. Rubinstein (2015). High-rate injection is associated with the increase in U.S. mid-continent seismicity, *Science* **348,** no. 6241, 1336–1340, doi: 10.1126/science.aab1345.

Wu, S.-M., K. M. Ward, J. Farrell, F.-C. Lin, M. Karplus, and R. B. Smith (2017). Anatomy of Old Faithful from subsurface seismic imaging of the Yellowstone Upper Geyser Basin, *Geophys. Res. Lett.* **44,** no. 20, 10,240–10,247, doi: 10.1002/2017GL075255.

Yu, C.-Q., W.-P. Chen, and R. D. van der Hilst (2013). Removing source-side scattering for virtual deep seismic sounding (VDSS), *Geophys. J. Int.* **195,** no. 3, 1932–1941, doi: 10.1093/gji/ggt359.

Zandt, G., and C. J. Ammon (1995). Continental crust composition constrained by measurements of crustal Poisson's ratio, *Nature* **374,** no. 6518, 152–154, doi: 10.1038/374152a0.

Zhan, Z., S. Ni, D. V. Helmberger, and R. W. Clayton (2010). Retrieval of Moho-reflected shear wave arrivals from ambient seismic noise, *Geophys. J. Int.* **182,** no. 1, 408–420, doi: 10.1111/j.1365-246X.2010.04625.x.

Zhu, H. (2018). Crustal wave speed structure of North Texas and Oklahoma based on ambient noise cross-correlation functions and adjoint tomography, *Geophys. J. Int.* **214,** 716–730, doi: 10.1093/gji/ggy169.

Zhu, L., and H. Kanamori (2000). Moho depth variation in southern California from teleseismic receiver functions, *J. Geophys. Res.* **105,** no. B2, 2969–2980, doi: 10.1029/1999JB900322.

Manuscript received 25 February 2020
Published online 28 October 2020